optica

Spontaneous photon-pair generation from a dielectric nanoantenna: supplementary material

GIUSEPPE MARINO[1,2,3,*], ALEXANDER S. SOLNTSEV[1,4], LEI XU[1,5,9], VALERIO F. GILI[3], LUCA CARLETTI[6], ALEXANDER N. PODDUBNY[1,7,8], MOHSEN RAHMANI[1], DARIA A. SMIRNOVA[1], HAITAO CHEN[1,5,9], ARISTIDE LEMAÎTRE[10], GUOQUAN ZHANG[9], ANATOLY V. ZAYATS[2], COSTANTINO DE ANGELIS[6], GIUSEPPE LEO[3], ANDREY A. SUKHORUKOV[1], AND DRAGOMIR N. NESHEV[1,*]

[1] *Nonlinear Physics Centre, Research School of Physics, Australian National University, Canberra ACT 2601, Australia*
[2] *Department of Physics and London Centre for Nanotechnology, King's College London, Strand, London WC2R 2LS, UK*
[3] *Matériaux et Phénomènes Quantiques, Université Paris Diderot-CNRS, F-75013 Paris, France*
[4] *School of Mathematical and Physical Sciences, University of Technology Sydney, 15 Broadway, Ultimo NSW 2007, Australia*
[5] *School of Engineering and Information Technology, University of New South Wales, Canberra ACT 2600, Australia*
[6] *Dept. of Information Engineering, University of Brescia, Via Branze 38, 25123 Brescia, Italy*
[7] *ITMO University, 49 Kronverksky Pr., Saint Petersburg 197101, Russia*
[8] *Ioffe Physical-Technical Institute, Saint Petersburg 194021, Russia*
[9] *The MOE Key Laboratory of Weak Light Nonlinear Photonics, School of Physics, Nankai University, Tianjin, China*
[10] *Centre de Nanosciences et de Nanotechnologies, CNRS, Universite Paris-Sud, Universite Paris-Saclay, C2N Marcoussis, F-91460, Marcoussis, France*

[*] *Corresponding author: E-mail: Giuseppe.Marino@univ-paris-diderot.fr, Dragomir.Neshev@anu.edu.au*

Published 4 November 2019

This document provides supplementary information to "Spontaneous photon-pair generation from a dielectric nanoantenna," https://doi.org/10.1364/optica.6.001416.

CONTENTS

1. PREDICTION OF BI-PHOTON RATE IN ALGAAS NANOCYLINDER

1.1. SPDC-SFG correspondence for localized nonlinear structure

We formulate and employ a general quantum-classical correspondence between spontaneous parametric down-conversion (SPDC) and sum-frequency generation (SFG) for arbitrary nanophotonic structures, drawing on the Green function formalism developed in [1, 2]. In Ref. [2], we have proved a general correspondence between the complex biphoton wavefunction and the amplitude of SFG process for arbitrary $\chi^{(2)}$-nonlinear nanostructure. Here we apply this proof for the case of nonlinear nanocylinder, when both the excitation and detection are done in the far field.

We start with calculating electric field of the structure illuminated by two plane waves, the "idler" one with the wave vector $-\boldsymbol{k}_i$ and the "signal" one with the wave vector $-\boldsymbol{k}_s$. To this end, we assume that both waves are generated by point dipoles located in the far field zone in the points $\boldsymbol{r}_{i,s} \parallel \boldsymbol{k}_{i,s}$, and having the unit amplitudes $\boldsymbol{d}_i^* \boldsymbol{e}_i^* \perp \boldsymbol{k}_i$ and $\boldsymbol{d}_s^* \parallel \boldsymbol{e}_s^* \perp \boldsymbol{k}_s$, respectively (Fig. S1). In this case, the linear fields at idler and signal frequencies can be written as

$$\boldsymbol{E}_{i,s}(\boldsymbol{r}) = G(\boldsymbol{r}, \boldsymbol{r}_{i,s}; \omega_{i,s}) \boldsymbol{d}_{i,s}^* \tag{S1}$$

where G is the electromagnetic Green function tensor satisfying the equation

$$\mathrm{rot}\,\mathrm{rot}\, G(\boldsymbol{r}, \boldsymbol{r}'; \omega) = \left(\frac{\omega}{c}\right)^2 \varepsilon(\boldsymbol{r}) G(\boldsymbol{r}, \boldsymbol{r}'; \omega) + 4\pi \left(\frac{\omega}{c}\right)^2 \delta(\boldsymbol{r} - \boldsymbol{r}'). \tag{S2}$$

Far away from the nonlinear structure, where $\varepsilon = 1$, the Green function reduces to the free Green function

$$G_{\alpha\beta} = \left[\left(\frac{\omega}{c}\right)^2 + \frac{\partial^2}{\partial x_\alpha \partial x_\beta}\right] \frac{\mathrm{e}^{\mathrm{i}\omega|\boldsymbol{r}-\boldsymbol{r}'|/c}}{|\boldsymbol{r} - \boldsymbol{r}'|}. \tag{S3}$$

The locally-plane idler and signal waves, incident upon the structure, are found by substituting Eq. Eq. (S3) into Eq. Eq. (S1) and assuming $r_{i,s} \gg r$. Hence, we find

$$\boldsymbol{E}_{i,s}^{(0)} = \frac{\mathrm{e}^{\mathrm{i}\omega_{i,s} r_{i,s}/c}}{r_{i,s}} q_{i,s}^2 \boldsymbol{d}_{i,s}^*, \tag{S4}$$

where $q_{i,s} = \omega_{i,s}/c$. The corresponding time-averaged intensities are given by

$$\Phi_{i,s} = \frac{c}{2\pi} |E_{i,s}^{(0)}|^2 = \frac{c}{2\pi} \frac{q_{i,s}^4}{r_{i,s}^2} |d_{i,s}|^2. \tag{S5}$$

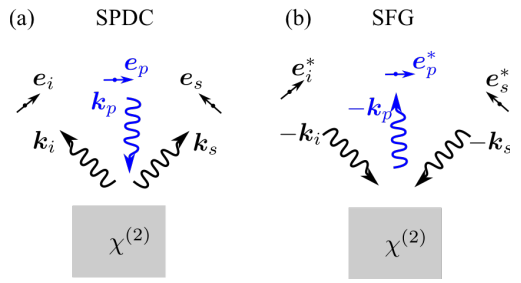

Fig. S1. Schematic illustration of reciprocal SPDC (a) and SFG (b) processes. Wave vectors $\boldsymbol{k}$ and polarizations $\boldsymbol{e}$ of signal (s), idler (i), and pump (p) waves are indicated.

The nonlinear SFG field as found as a convolution of the $\chi^{(2)}$ susceptibility, the incident fields, and the Green function at the sum frequency

$$E_\alpha^{(\mathrm{SFG})}(\boldsymbol{r}_p \leftarrow \boldsymbol{r}_i, \boldsymbol{d}_i^*; \boldsymbol{r}_s, \boldsymbol{d}_s^*) = \int \mathrm{d}^3 r' G_{\alpha\beta}(\boldsymbol{r}_p, \boldsymbol{r}') \chi^{(2)}_{\gamma\delta,\beta} G_{\gamma\nu}(\boldsymbol{r}', \boldsymbol{r}_i) G_{\delta\mu}(\boldsymbol{r}', \boldsymbol{r}_s) d_{i,\nu}^* d_{s,\mu}^*. \tag{S6}$$

Here, $\alpha, \beta, \gamma, \delta, \mu, \nu$ are the Cartesian indices. The frequency arguments of the Green functions are omitted for the sake of brevity. It is instructive to present the Green functions in the following way

$$G_{\alpha\beta}(\boldsymbol{r}, \boldsymbol{r}') = q^2 \frac{\mathrm{e}^{\mathrm{i}qr}}{r} g_{\alpha\beta}\left(\tfrac{\boldsymbol{r}}{r}, \boldsymbol{r}'\right) \text{ for } r \gg c/\omega, r \gg r', \tag{S7}$$

where the dimensionless scattering amplitudes $g_{\alpha\beta}(\frac{\boldsymbol{r}}{r}, \boldsymbol{r}') \equiv g_{\alpha\beta}(\boldsymbol{k}, \boldsymbol{r}')$ describe the conversion between the near field at the point $\boldsymbol{r}'$ and the plane wave propagating in the direction $\boldsymbol{r}/r \parallel \boldsymbol{k}$. We also use the Lorentz reciprocity property

$$G_{\alpha\beta}(\boldsymbol{r}, \boldsymbol{r}') = G_{\beta\alpha}(\boldsymbol{r}', \boldsymbol{r}). \tag{S8}$$

Applying Eq. Eq. (S7) and Eq. Eq. (S8) to Eq. Eq. (S6), we rewrite the sum-frequency wave as

$$E_\alpha^{(\mathrm{SFG})}(\boldsymbol{r}_p \leftarrow \boldsymbol{r}_i, \boldsymbol{d}_i^*; \boldsymbol{r}_s, \boldsymbol{d}_s^*) = \frac{q_i^2 q_s^2 q_p^2}{r_i r_s r_p} \mathrm{e}^{\mathrm{i}(q_i r_i + q_s r_s + q_p r_p)} \int \mathrm{d}^3 r' g_{\alpha\beta}(\boldsymbol{k}_p, \boldsymbol{r}') \chi^{(2)}_{\gamma\delta,\beta} g_{\nu\gamma}(\boldsymbol{k}_i, \boldsymbol{r}') g_{\mu\delta}(\boldsymbol{k}_s, \boldsymbol{r}') d_{i,\nu}^* d_{s,\mu}^*. \tag{S9}$$

Now we introduce the differential SFG efficiency as

$$\mathrm{d}\Xi^{\mathrm{SFG}}(-\boldsymbol{k}_i, \boldsymbol{e}_i^*; -\boldsymbol{k}_s \boldsymbol{e}_s^* \to -\boldsymbol{k}_p, \boldsymbol{e}_p^*) = r_p^2 \mathrm{d}\Omega_p \frac{\Phi_p(-\boldsymbol{k}_p, \boldsymbol{e}_p^*)}{\Phi_i(-\boldsymbol{k}_i, \boldsymbol{e}_i^*) \Phi_s(-\boldsymbol{k}_s, \boldsymbol{e}_s^*)}, \tag{S10}$$

i.e., it is the ratio of the power of SFG photons propagating inside the solid angle $\mathrm{d}\Omega_p$ in the direction $-\boldsymbol{k}_i$ to the intensities of incoming signal and idler plane waves Φ_i and Φ_s. Eq. (S10) bears analogies with the scattering cross section in the linear problem. The SFG efficiency is found from Eq. (S9) and Eq. (S10) as

$$\frac{\mathrm{d}\Xi^{\mathrm{SFG}}(-\boldsymbol{k}_i, \boldsymbol{e}_i^*; -\boldsymbol{k}_s \boldsymbol{e}_s^* \to -\boldsymbol{k}_p, \boldsymbol{e}_p^*)}{\mathrm{d}\Omega_p} = \frac{2\pi q_p^4}{c} \times \left| \int \mathrm{d}^3 r' e_{p,\alpha} g_{\alpha\beta}(\boldsymbol{k}_p, \boldsymbol{r}') \chi^{(2)}_{\gamma\delta,\beta} g_{\nu\gamma}(\boldsymbol{k}_i, \boldsymbol{r}') g_{\mu\delta}(\boldsymbol{k}_s, \boldsymbol{r}') e_{i,\nu}^* e_{s,\mu}^* \right|^2. \tag{S11}$$

Now we proceed to the SPDC process. The complex wavefunction of a photon pair, generated in a $\chi^{(2)}$-nonlinear structure, has the amplitude [1]

$$T(\boldsymbol{r}_s \mu, \boldsymbol{r}_i \nu \leftarrow \boldsymbol{r}_p \boldsymbol{e}_p) = \int \mathrm{d}^3 r' G_{\sigma_s \nu}(\boldsymbol{r}_s, \boldsymbol{r}') G_{\sigma_i \nu}(\boldsymbol{r}_i, \boldsymbol{r}') \chi^{(2)}_{\gamma\delta,\beta}(\boldsymbol{r}') E_{p,\beta}(\boldsymbol{r}', \omega_p), \tag{S12}$$

where $\boldsymbol{r}_s(\boldsymbol{r}_i)$ and $\mu(\nu)$ are signal (idler) photon coordinates and polarizations, respectively, and E_p is the electric field of the pump with the frequency ω_p. Similar to Eq. Eq. (S1), in the SFG case, we now write that the pump wave is generated by the point far-field source

$$\boldsymbol{E}_p(\boldsymbol{r}) = G(\boldsymbol{r}, \boldsymbol{r}_p) \boldsymbol{d}_p. \tag{S13}$$

where $\boldsymbol{d}_p \parallel \boldsymbol{e}_p \perp \boldsymbol{r}_p$ is the point dipole amplitude. Plugging in the Green function asymptotic expressions in Eq. Eq. (S7), we rewrite the biphoton wavefunction in the form

$$T(\boldsymbol{r}_s\mu, \boldsymbol{r}_i\nu \leftarrow \boldsymbol{r}_p\boldsymbol{e}_p) = \frac{q_i^2 q_s^2 q_p^2}{r_i r_s r_p} \mathrm{e}^{\mathrm{i}(q_i r_i + q_s r_s + q_p r_p)} \int \mathrm{d}^3 r' g_{\alpha\beta}(\boldsymbol{k}_p, \boldsymbol{r}') \chi^{(2)}_{\gamma\delta,\beta} g_{\nu\gamma}(\boldsymbol{k}_i, \boldsymbol{r}') g_{\mu\delta}(\boldsymbol{k}_s, \boldsymbol{r}') d_{p,\alpha}. \quad \text{(S14)}$$

Comparing Eq. Eq. (S14) with Eq. Eq. (S9), we see that

$$T(\boldsymbol{r}_s\mu, \boldsymbol{r}_i\nu \leftarrow \boldsymbol{r}_p\boldsymbol{e}_p) d^*_{s,\mu} d^*_{i,\nu} = E^{(\mathrm{SFG})}_\alpha(\boldsymbol{r}_p \leftarrow \boldsymbol{r}_i, \boldsymbol{d}^*_i; \boldsymbol{r}_s, \boldsymbol{d}^*_s) d_{p,\alpha}, \quad \text{(S15)}$$

which proves the SPDC-SFG correspondence for the considered problem.

We are also interested in comparing the experimentally accessible quantities, namely, the two-photon pair generation rate and the SFG generation efficiency defined in Eq. Eq. (S11). In order to determine the photon pair generation rate, we need to calibrate the photon detection process [1, 2]. To this end, we explicitly introduce the signal and idler detectors modelled as the two-level systems with the dipole momenta matrix elements $\boldsymbol{d}_i$, $\boldsymbol{d}_s$ and the energies $\hbar\omega_i$, $\hbar\omega_s$. The number of photons absorbed by the detector per unit time is given by

$$\frac{\mathrm{d}N_{\mathrm{abs}}}{\mathrm{d}t} = \frac{2\pi}{\hbar} \delta(\hbar\omega - \hbar\omega_{i,s}) |\boldsymbol{d} \cdot \boldsymbol{E}_{i,s}|^2, \quad \text{(S16)}$$

where $\boldsymbol{E}_{i,s} \propto 1/r_{i,s}$ is the local electric field of emitted signal or idler photon at the corresponding detector. The detector quantum efficiency $\mathrm{d}QE_{i,s}/\mathrm{d}\Omega_{i,s}$ is the ratio between the number of photons absorbed by the detector and the number of photons $\mathrm{d}N_{i,s}/\mathrm{d}t$ propagating inside the solid angle $\mathrm{d}\Omega_{i,s}$ per unit time

$$\frac{\mathrm{d}N_{i,s}}{\mathrm{d}t} = r^2 \mathrm{d}\Omega_{i,s} \frac{c}{2\pi\hbar\omega_{i,s}} |E|^2, \quad \text{(S17)}$$

$$\frac{\mathrm{d}QE_{i,s}}{\mathrm{d}\Omega_{i,s}} = \frac{\mathrm{d}N_{\mathrm{abs}}}{\mathrm{d}N_{i,s}} = \frac{4\pi\omega |d_{i,s}|^2}{\hbar c} \frac{1}{r^2_{i,s}}. \quad \text{(S18)}$$

The two-photon generation rate per unit of the signal and idler spectra is formally defined as

$$\frac{\mathrm{d}N_{\mathrm{pair}}}{\mathrm{d}t \mathrm{d}\omega_i \mathrm{d}\omega_s \mathrm{d}\Omega_i \mathrm{d}\Omega_s} = \frac{W_{is}}{\mathrm{d}QE_i \mathrm{d}QE_s}, \quad \text{(S19)}$$

where

$$W_{is} = \frac{2\pi}{\hbar} \delta(\hbar\omega_p - \hbar\omega_i - \hbar\omega_s) |\sum_{\nu\mu} d^*_{i,\nu} d^*_{s,\mu} T(\boldsymbol{r}_s\mu, \boldsymbol{r}_i\nu \leftarrow \boldsymbol{r}_p\boldsymbol{e}_p)|^2, \quad \text{(S20)}$$

is the uncalibrated rate of two photon counts calculated from the bi-photon amplitude Eq. Eq. (S14). Substituting Eqs. Eq. (S14),Eq. (S18),Eq. (S20) into Eq. Eq. (S19) and comparing with Eq. Eq. (S11), we find a general *absolute* correspondence between the sum frequency rate and the photon pair generation rate in the form

$$\frac{1}{\Phi_p} \frac{\mathrm{d}N_{\mathrm{pair}}(\boldsymbol{k}_i, \boldsymbol{e}_i; \boldsymbol{k}_s\boldsymbol{e}_s \leftarrow \boldsymbol{k}_p, \boldsymbol{e}_p)}{\mathrm{d}t \mathrm{d}\Omega_i \mathrm{d}\Omega_s \mathrm{d}\omega_i \mathrm{d}\omega_s} = \frac{\delta(\omega_i + \omega_s - \omega_p)}{2\pi} \frac{\lambda_p^4}{\lambda_i^3 \lambda_s^3} \frac{\mathrm{d}\Xi^{\mathrm{SFG}}(-\boldsymbol{k}_i, \boldsymbol{e}^*_i; -\boldsymbol{k}_s\boldsymbol{e}^*_s \to -\boldsymbol{k}_p, \boldsymbol{e}^*_p)}{\mathrm{d}\Omega_p}, \quad \text{(S21)}$$

where Φ_p is the SPDC pump flux. Equation Eq. (S21) is the main result for the SPDC-SFG correspondence, valid for an arbitrary localized $\chi^{(2)}$-nonlinear system. In order to facilitate comparison with actual experimental setup, we first integrate it over the signal and idler frequencies, neglecting the dispersion effects, and obtain

$$\frac{1}{\Phi_p} \frac{\mathrm{d}N_{\mathrm{pair}}(\boldsymbol{k}_i, \boldsymbol{e}_i; \boldsymbol{k}_s\boldsymbol{e}_s \leftarrow \boldsymbol{k}_p, \boldsymbol{e}_p)}{\mathrm{d}t \mathrm{d}\Omega_i \mathrm{d}\Omega_s} = \frac{\Delta\omega_s}{2\pi} \frac{\lambda_p^4}{\lambda_i^3 \lambda_s^3} \frac{\mathrm{d}\Xi^{\mathrm{SFG}}(-\boldsymbol{k}_i, \boldsymbol{e}^*_i; -\boldsymbol{k}_s\boldsymbol{e}^*_s \to -\boldsymbol{k}_p, \boldsymbol{e}^*_p)}{\mathrm{d}\Omega_p}, \quad \text{(S22)}$$

where $\Delta\omega_s \equiv 2\pi c \Delta\lambda_s/\lambda_s^2$ is the signal spectral width. Further simplification can be made if the polarization degree of freedom is disregarded and it is assumed that the radiation is homogeneously distributed in all the half-space, i.e., $\mathrm{d}\Omega \to 2\pi$. This simplification yields an expression

$$\frac{1}{\Phi_p} \frac{\mathrm{d}N_{\mathrm{pair}}}{\mathrm{d}t} = 2\pi \frac{c\Delta\lambda_s}{\lambda_s^2} \frac{\lambda_p^4}{\lambda_i^3 \lambda_s^3} \Xi^{\mathrm{SFG}}, \quad \text{(S23)}$$

that is equivalent to Eq. (1) in the main text.

1.2. Numerical estimation for a nanocylinder

Now we apply the general result for the SPDC-SFG correspondence Eq. Eq. (S23) to the experimental configuration studied here. Let us write the pump intensity in terms of the pump electromagnetic power per unit area, therefore, Eq. Eq. (S23) takes the form

$$\frac{dN_{\mathrm{pair}}}{dt} = 2\pi \frac{c\Delta\lambda_s}{\lambda_s^2} \frac{\lambda_p^4}{\lambda_s^3 \lambda_i^3} \Xi^{\mathrm{SPDC}}_{\mathrm{avg}} \frac{\langle P_{\mathrm{pump,SPDC/disk}} \rangle}{A_{\mathrm{pump,SPDC}}}, \quad \text{(S24)}$$

where $\frac{\langle P_{\mathrm{pump,SPDC/disk}} \rangle}{A_{\mathrm{pump,SPDC}}}$ is the SPDC pump flux Φ_p of Eq. Eq. (S23), with $\langle P_{\mathrm{pump,SPDC/disk}} \rangle = \langle P_{\mathrm{pump,SPDC}} \rangle \times P^{\mathrm{pump,SPDC}}_{mode\%}$ being the average power at the disk, $\langle P_{\mathrm{pump,SPDC}} \rangle = 2.2$ mW being the incident average power at the SPDC pump frequency, $P^{pump}_{mode\%} = 44\%$ being the simulated percentage of power coupled to the mode at the SPDC frequency, and $A_{\mathrm{pump,SPDC}}$ being the disk area. The modal average of the dimensional SFG efficiency can be calculated as

$$\Xi^{\mathrm{SFG}}_{\mathrm{avg}} = \frac{\langle P_{SFG} \rangle}{\langle \Phi_i \Phi_s \rangle} = \langle P_{SFG} \rangle \left(\frac{\langle P_i P_s \rangle}{A^2_{\mathrm{pump,SFG}}} \right)^{-1} = \langle P_{SFG} \rangle \left(\frac{\langle P_{\mathrm{pump,SFG/disk}} \rangle P^{\mathrm{pump,SFG}}_{peak/disk}}{\sqrt{2} A^2_{\mathrm{pump,SFG}}} \right)^{-1}, \quad \text{(S25)}$$

where $\langle P_{SFG} \rangle = \frac{Counts_{cam}}{Counts/W} (T^{SFG}_{obj} T^{SFG}_{dm})^{-1}$ is the average SFG power emitted by the nanocylinder, with $Counts_{cam}$ the number of counts collected by the camera at an integration time of 0.0005 sec, and $Counts/W$ the calibrated number of counts per Watt corresponding to this time, while T^{SFG}_{obj} and T^{SFG}_{dm} are transmission through objective and dichroic mirror, respectively, which are set in the detection path. On the other hand, $\langle \Phi_i \Phi_s \rangle$ and $\langle P_i P_s \rangle$ are the scalar products of signal and idler energy fluxes and powers, respectively, $\langle P_{\mathrm{pump,SFG/disk}} \rangle = \langle P_{\mathrm{pump,SFG}} \rangle P^{\mathrm{pump,SFG}}_{mode\%}$ is the SFG pump average power at the

nanocylinder, with $\langle P_{\text{pump,SFG}} \rangle = 2.6mW$ being the average incident power, and $P^{\text{pump,SFG}}_{mode\%} = 68\%$ being the simulated percentage of power coupled to the mode at the SFG pump frequency. Finally $P^{\text{pump,SFG}}_{peak/disk} = P^{\text{pump,SFG}}_{avg/disk}/(\Delta T/T)$ is the fundamental peak power, with $\Delta T = 100fs$ being the pulse duration and $1/T = 80$ MHz the repetition rate. The factor of $\sqrt{2}$ in the denominator accounts for the difference between peak and average powers under the assumption of a Gaussian transform-limited pulse.

It is interesting to note that in order to compare the dimensional SFG efficiency associated to Eq. Eq. (S25), i.e. $\langle P_{SFG} \rangle / \langle P_{\text{pump,SFG/disk}} \rangle = 2.6 * 10^{-7}$, with data given in the literature for SHG, we need to substitute $P^{\text{pump,SFG}}_{mode\%}$ with the ratio $Area_{disk}/Area_{spot}$, which results in an efficiency of $1.8 * 10^{-5}$.

Application of the given definitions for Eq. Eq. (S24) leads to a biphoton rate of the order of 380 Hz.

The discrepancy between the experimental, estimated from 30 to 210 Hz, and predicted rate of generated photon pairs can be attributed to the lack of a strict reversibility between the quantum and classical setup, as mentioned in the main text. Nevertheless, the predicted rate through the SFG experiments remains of crucial interest when one wants to estimate the order of magnitude of the SPDC process efficiency and its detectability above the dark count rate of a single photon detector.

2. CHARACTERISATION OF RESONANT DIELECTRIC NANOANTENNAS

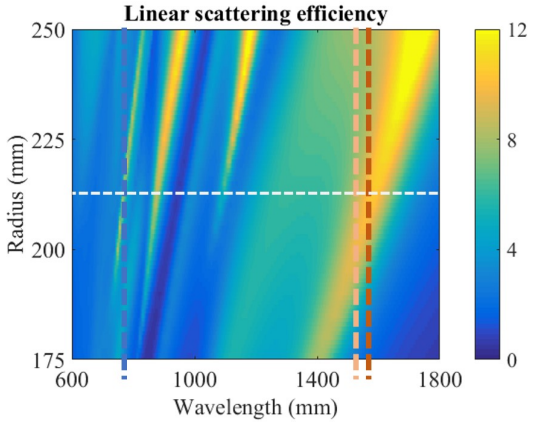

Fig. S2. Dependence of the linear scattering efficiency on the radius of the AlGaAs nanodisks, for a fixed height of 400 nm. The vertical blue and orange lines show the spectral ranges of the pump light and the generated SPDC light (signal and idler), respectively. The horizontal white line corresponds to the case of Figure 1c.

The resonances of the AlGaAs nanoantennas depend significantly on the size of the nanodisks, which might vary slightly in the fabrication. Figure S2 shows the calculated linear scattering efficiency of the AlGaAs nanoantennas for different radii and a fixed height of 400 nm. With increasing of the disk radius, the resonances move towards longer wavelengths.

To assure that our fabricated antennas are indeed resonant to the participating wavelengths (pump, signal and idler), we have further recorded linear scattering spectra for slightly different radii (see Fig. S3a,b). A dark/bright field microscopy is carried out around the pump, signal and idler frequencies, respectively, from a metasurface made out of an array of nanoantennas. VIS/NIR light from a halogen lamp is focused by a dark/bright-field objective 100× 0.85 NA / 20× 0.25 NA. The reflected signal is collected by the same objective and directed to a VIS/NIR spectrometer. The dark-field illumination allows to drastically reduce both the noise from the substrate (at wavelengths below 890 nm) and from the large band-edge luminescence of the metasurface [3] (see violet shadow area at wavelengths below 730 nm). The metasurface, while preserving the nature of the modes of the isolated nanoantenna, allows for a constructive interference in the zero order [4].

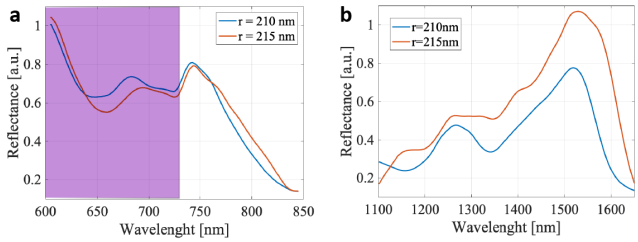

Fig. S3. (a) Dark and (b) bright field microscopies around the pump/ signal and idler frequencies from a metasurface made out of an array of nanoantennas. The violet shadow area at wavelengths below 730 nm represents represents the absorption window of the AlGaAs

While the results in Fig. S3 indicate the resonant behaviour of the fabricated nanoantennas, we have further selected the best resonant nanoantenna (out of several nominally identical nanoantennas) by choosing the antenna providing highest SHG signal. As the SHG process is nonlinear in nature, it is highly sensitive to variations in the resonant behaviour.

Finally, the SFG measurements in Fig. 2c, confirm that the signal and idler wavelengths are positioned exactly at the middle of the resonance dip. As also indicated in Ref. [5], the individual SHG intensities of the signal and idler are equal only at the resonance. Any detuning from the resonance would result in asymmetry of the spectral features in Fig. 2c.

3. SFG EXPERIMENTAL SETUP

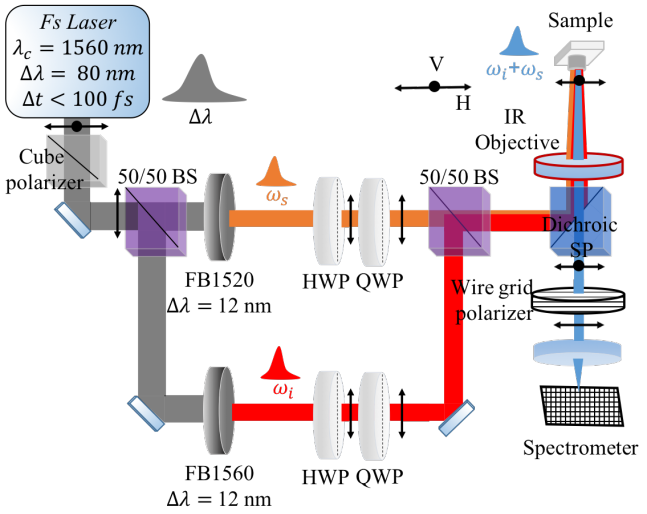

Fig. S4. Schematic of the SFG experimental setup. A camera calibrated by a power meter was used in place of a spectrometer to measure the SFG efficiency and directionality diagrams.

4. SIMULATED SFG POLARIZATION DEPENDENCE AND DIRECTIONALITY DIAGRAMS

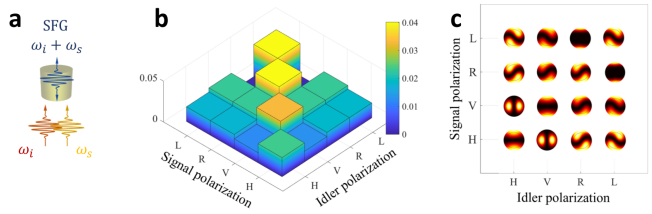

Fig. S5. (a) Schematic of the SFG process. (b) Intensity of H-polarized reflected SFG at 770 nm simulated with 16 combinations of horizontal (H), vertical (V), right circular (R) and left circular (L) polarizations of signal and idler beams for the nanocylinder geometry in Fig. 2. (c) Simulated reflected SFG directionality diagrams for the polarization combinations shown in (b) and an $NA = 0.7$.

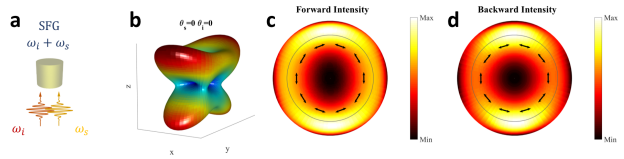

Fig. S6. (a) Schematic of the SFG process at normal incidence. (b) Calculated SFG radiation pattern, polarised in y (V) direction, for normal incidence of the signal and idler photons. (c,d) Projection of the radiation pattern in forward and backward directions, respectively. The arrows indicated the polarisation of the emitted SFG light. The dotted circles indicate the numerical aperture of our collection objective of $NA = 0.7$.

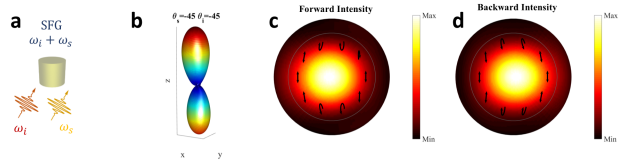

Fig. S7. (a) Schematic of the SFG process for oblique incidence at 45°. (b) Calculated SFG radiation pattern, polarised in y (V) direction, for oblique incidence of the signal and idler photons. (c,d) Projection of the radiation pattern in forward and backward direction, respectively. The arrows indicate the polarisation of the emitted SFG light. The dotted circles indicate the numerical aperture of our collection objective of $NA = 0.7$.

5. SPDC EXPERIMENTAL SETUP

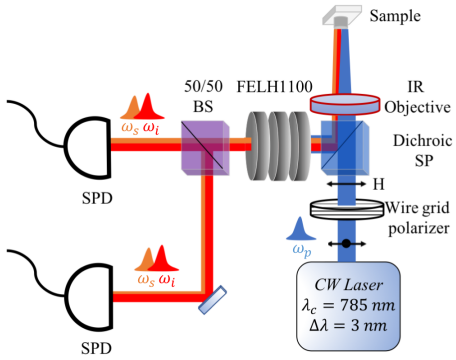

Fig. S8. Schematic of SPDC experimental setup. SPD - Single photon detectors. Dichroic SP - short-pass dichroic beam splitter.

6. BI-PHOTON RATE FROM ALGAAS NANOCYLINDER ON A SUBSTRATE

The measured time difference histogram for the AlGaAs nanoresonator on AlOx/GaAs substrate is illustrated in Fig. 3(a). Correlation due to thermal excitation of the semiconductor material has been fitted with a Gaussian curve. The rate of detected thermal photon pairs is

$$\frac{dN^{th,det}_{\text{disk+sub}}}{dt} = \frac{Area_{\text{disk+sub}}}{t}, \tag{S26}$$

where $Area(Counts) = \frac{a*c*\sqrt{\pi}}{w_{bin}}$, with $a = (888 \pm 224) Counts$, being the peak coincidence counts calculated from the Gaussian fit with a confidence interval of 95%, $c = 0.839$ ns, being the FWHM of the Gaussian curve, w_{bin}=162 ps being the size of the clock period (native bin) of the time to digital converter, and t=24h being the integration time. Considering that losses in detection can be estimated as

$$\zeta^{TOT}_{signal/idler} = \zeta^{obj}_{signal/idler} \times \zeta^{filters}_{signal/idler} \times \zeta^{mirrors}_{signal/idler} \times \zeta^{fibers}_{signal/idler} \times \zeta^{\eta_{quant}}_{signal/idler} = 0.0003, \quad \text{(S27)}$$

where $\zeta^{obj}_{signal/idler} = 0.5^2$ and $\zeta^{filters}_{signal/idler} = 0.85^6$ are photon pairs transmissions through the objective and three long pass filters, respectively. $\zeta^{mirrors}_{signal/idler} = 0.96^{10}$ is the reflection of photon pairs through mirrors, $\zeta^{fibers}_{signal/idler} = 0.66^2$ is the fibre coupling efficiency, and $\zeta^{\eta_{quant}}_{signal/idler} = 0.1^2$ is the quantum efficiency of the single photon detector. Considering the transmittance of each individual optical element as an independent variable with an uncertainty of 5%. Then, the uncertainty of the total transmission through 22 optical elements is $\sqrt{(22)} * 5\% = 4.69 * 5\% = 23\%$. It follows that the generated thermal bi-photon rate is

$$\frac{dN^{th}_{\text{disk+sub}}}{dt} = \frac{dN^{th,det}_{\text{disk+sub}}}{dt} (\zeta^{TOT}_{signal/idler})^{-1} = 345 \pm 87 \text{ Hz}. \quad \text{(S28)}$$

SPDC correlation, emerging from both the correlation due to the thermal excitation and the background, can be then extracted by central bin counts on top of the Gaussian fit, i.e. 872 Counts at time 26.5 ns of the coincidence histogram. Finally, the generated SPDC bi-photon rate results:

$$\frac{dN^{SPDC}_{\text{disk+sub}}}{dt} = \frac{Counts^{central,bin}_{\text{disk+sub}}}{t} (\zeta^{TOT}_{signal/idler})^{-1} = 34 \text{ Hz}. \quad \text{(S29)}$$

This figure is higher than the dark count rate of the single photon detectors, being 5 Hz for an efficiency of 10% and a temperature of $-90°C$.

We can then define the SPDC efficiency of the AlGaAs nanoantenna as the ratio between the number of photon pairs generated per second, $N^{gen}_{\text{disk+sub}}$, and the number of photons pumped per second, N^{pump}:

$$\frac{N^{SPDC}_{\text{disk+sub}}}{N^{pump}} = 2.4 \cdot 10^{-15}. \quad \text{(S30)}$$

7. BI-PHOTON RATE FROM THE SUBSTRATE

Figure S9 illustrates the measured time difference histogram for the AlOx/GaAs substrate only and a Gaussian fit curve. The rate of detected thermal photon pairs is

$$\frac{dN^{th,det}_{\text{sub}}}{dt} = \frac{Area_{sub}}{t} = 0.037 Hz, \quad \text{(S31)}$$

where $Area(Counts) = a\, c\, \sqrt{\pi}/w_{bin}$, with $a = 371 \pm 134\, Counts$ being the peak coincidence counts calculated from the Gaussian fit with a confidence interval of 95%, c=0.839 ns being the FWHM of the Gaussian curve, w_{bin}=162 ps being the size of the clock period (native bin) of the time to digital converter, and $t = 12$ h being the integration time. It follows that the generated thermal bi-photon rate is

$$\frac{dN^{th}_{\text{sub}}}{dt} = \frac{dN^{th,det}_{\text{sub}}}{dt} (\zeta^{TOT}_{signal/idler})^{-1} = 135 \pm 50 Hz, \quad \text{(S32)}$$

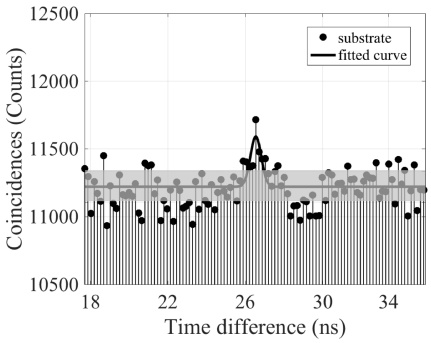

Fig. S9. Measured SPDC coincidences counts from the AlOx/GaAs substrate integrated over 12 h via the experimental setup illustrated in Fig. S8.

Even in this case, SPDC correlation can be extracted from the central bin counts on top of the Gaussian fit, i.e. 118 counts at time 26.5 ns of the coincidence histogram. Finally, the generated SPDC bi-photon rate from the substrate is

$$\frac{dN^{SPDC}_{\text{sub}}}{dt} = \frac{Counts^{central,bin}_{sub}}{t} (\zeta^{TOT}_{signal/idler})^{-1} = 9 \text{ Hz}. \quad \text{(S33)}$$

This value is of the order of the noise level in the background, indicating that a possible SPDC from the substrate is very weak.

8. INFLUENCE OF ALGAAS NANOCYLINDER ON THE SPDC PROCESS FROM ALOX/GAAS SUBSTRATE

In order to estimate the influence of an AlGaAs disk on the SPDC process from the AlOx/GaAs substrate, we make use of the reciprocity of the SPDC process, and numerically calculate the diffraction pattern caused by the disk in the reversed geometry: a plane wave at the signal/idler wavelength obliquely incident from the air side on the structure. As reported in Fig. S10 (a,b,c,d), the field distributions for incident angles of 0, $\pi/12$, $\pi/6$, $\pi/4$, respectively, do not show hot spots being formed in the AlOx/GaAs substrate. Hence, the presence of the AlGaAs disk does not increase the background SPDC photons generated from the substrate. To further estimate the influence of an

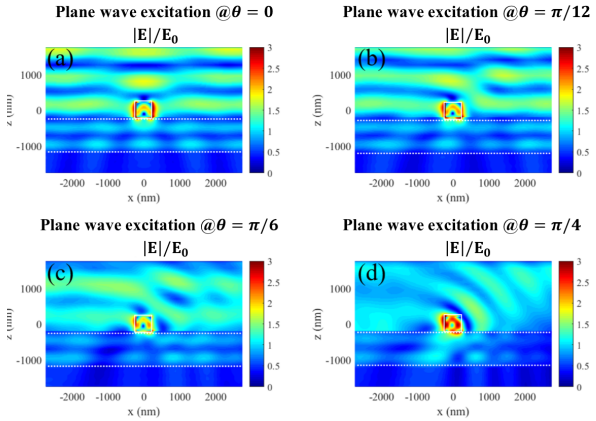

Fig. S10. The field distributions for incident angles (a) 0, (b) $\pi/12$, (c) $\pi/6$, and (d) $\pi/4$ at a signal/idler wavelength of λ=1550 nm. White dashed lines depict the substrate interfaces.

AlGaAs disk on the SPDC process from the AlOx/GaAs substrate, we numerically calculate the scattering at the signal/idler wavelength of an electric dipole placed in the proximity of the AlOx/GaAs substrate. Figure S11 shows the corresponding field distributions for a horizontally (a,b) and vertically-oriented (c,d) dipole with (a,c) and without (b,d) the AlGaAs disk, respectively. The total emission power from the horizontally-oriented dipole increases by 0.45% in the presence of the nanocylinder, while the power collected by a microscope objective with $NA = 0.7$ is about 0.48% in (a), and 0.4% in (b). In the case of a vertically-oriented dipole source, instead, the total emission power in the bare film structure (c) differs from the structure with AlGaAs disk (d) by less than 0.1% due to the suppression of the dipole emission along z, thereby resulting in a weaker coupling to the AlGaAs disk resonances compared to the horizontally-oriented dipole case. Moreover, the power collected by a microscope objective with NA=0.7 is about 0.4% in (c) and 0.5% in (d).

From both the two numerical calculations illustrated above, it follows that the AlGaAs disk will have little influence on the SPDC emission rate from the AlOx/GaAs substrate.

9. FIGURE OF MERIT FOR SPDC EFFICIENCY

The experimentally observed SPDC rate of 34 Hz is modest in itself, but not when the pump energy stored by the nanoantenna is taken into account. The corresponding figure of merit for SPDC efficiency results $dN/dt \cdot (V_0 I_p Q_p)^{-1}$, where V_0 is the volume of the nonlinear material responsible for SPDC, I_p is the incident pump intensity at the input, and Q_p is the quality factor at the pump wavelength, to account for higher pump intensity inside the nonlinear resonator, compared to the incident pump intensity. Such a figure of merit for an AlGaAs nanocylinder with $V_0 \sim 0.4\,\mu m^3$, $I_p \sim 1.2\ mW/\mu m^2$, $Q_p \sim 52$ is 1.4 GHz/Wm, being 4 orders of magnitude higher than the substrate source with $V_0 \sim 4.7\,\mu m^3$, $I_p \sim 1.2\ mW/\mu m^2$, $Q_p \sim 1$, three orders of magnitude higher than the value achieved in typical bulk optics based on nonlinear crystals, such as 50 Hz in BBO with $V_0 \sim 10\ mm^3$, $I_p \sim 50\ mW/mm^2$, $Q_p \sim 1$ [6] and about 10 times higher compared to leading parametric down-conversion on-chip sources of up to 3MHz rate with $V_0 \sim 200\ \mu m^3$, $I_p \sim 1\ mW/\mu m^2$, $Q_p \sim 1.1 * 10^5$ [7].

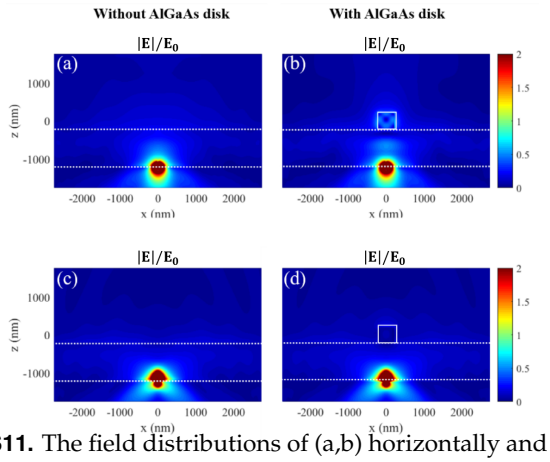

Fig. S11. The field distributions of (a,b) horizontally and (c,d) vertically-oriented dipoles placed in the proximity of AlOx/GaAs substrate at a signal/idler wavelength of 1550 nm with (a,c) and without (b,d) AlGaAs disk on top, respectively. White dashed lines delimite the substrate interfaces.

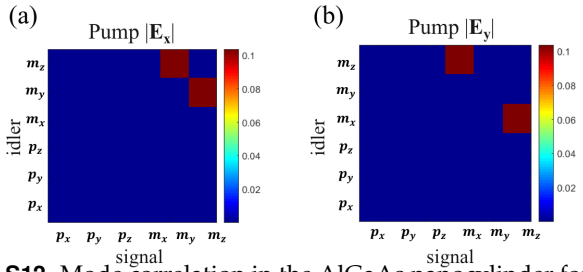

Fig. S12. Mode correlation in the AlGaAs nanocylinder for H (left) and V (right) polarized pump excitation.

10. MODE CORRELATION IN ALGAAS NANOCYLINDER

We further estimate the mode correlation during the SPDC process from AlGaAs nanocylinder. Based on the calculated scattering efficiency as shown in Fig. 1(c) in the main text, the electric field inside the nanoparticle can be well approximated by a superposition of ED and MD modes

$$\mathbf{E}_{\text{in}}^{(\omega)} \approx E_0 \left[\frac{1}{k(\omega)} (a_{1,1} - a_{1,-1}) \mathbf{E}(p_x) + \frac{1}{k(\omega)} (a_{1,1} + a_{1,-1}) \mathbf{E}(p_y) - \frac{1}{k(\omega)} \sqrt{2} a_{1,0} \mathbf{E}(p_z) + (b_{1,1} - b_{1,-1}) \mathbf{E}(m_x) + (b_{1,1} + b_{1,-1}) \mathbf{E}(m_y) + \sqrt{2} b_{1,0} \mathbf{E}(m_z) \right], \tag{S34}$$

where

$$\begin{aligned}
\mathbf{E}(p_x) &= \nabla \times j_1(k(\omega)r) \left(\mathbf{X}_{1,1}(\theta,\phi) - \mathbf{X}_{1,-1}(\theta,\phi) \right) /2\text{i}, \\
\mathbf{E}(p_y) &= \nabla \times j_1(k(\omega)r) \left(\mathbf{X}_{1,1}(\theta,\phi) + \mathbf{X}_{1,-1}(\theta,\phi) \right) /2, \\
\mathbf{E}(p_z) &= -\nabla \times j_1(k(\omega)r) \mathbf{X}_{1,0}(\theta,\phi) / \sqrt{2}, \\
\mathbf{E}(m_x) &= j_1(k(\omega)r) \left(\mathbf{X}_{1,1}(\theta,\phi) - \mathbf{X}_{1,-1}(\theta,\phi) \right) /2\text{i}, \\
\mathbf{E}(m_y) &= j_1(k(\omega)r) \left(\mathbf{X}_{1,1}(\theta,\phi) + \mathbf{X}_{1,-1}(\theta,\phi) \right) /2, \\
\mathbf{E}(m_z) &= -j_1(k(\omega)r) \mathbf{X}_{1,0}(\theta,\phi) / \sqrt{2},
\end{aligned}$$

are the corresponding electric fields for ED and MD modes with different orientations along x, y, z directions, respectively. Here, $k(\omega) = k_0 \sqrt{\varepsilon(\omega)}$ is wavenumber in the medium, $k_0 = \omega/c$, $j_1(k(\omega)r)$ is spherical Bessel function of order $l = 1$, $\mathbf{X}_{1,1}(\theta,\phi)$ are vector spherical harmonics (in the spherical coordinate system associated with z axis), $a_{1,\pm1}$ and $b_{1,\pm1}$ are the excitation coefficients.

We estimate the sub-wavelength mode correlation responsible for the generation of signal and idler photon pairs (Fig. S12) by calculating the SFG normal output when exciting the idler and signal fields with combination of ED (p_x or p_y or pz) and MD (m_x or m_y or m_z) inside the disk at idler or signal wavelengths, respectively.

As can be seen from Fig. S12, with $\boldsymbol{E}_H \parallel y$ ($\boldsymbol{E}_V \parallel x$) pump, the generated two photons are dominantly coupled into m_x and m_z (m_y and m_z) modes, respectively. Due to the SFG-SPDC correspondence, the SFG process has the same symmetry properties and can be understood using the group theory [8]. At the signal/idler frequency, the electric field is controlled by the magnetic dipole resonance, while at the pump/SFG frequency it is determined by the electric dipole mode. In the T_d symmetry group of the AlGaAs crystalline lattice, the magnetic dipole modes transform according to the F_1 irreducible representation,

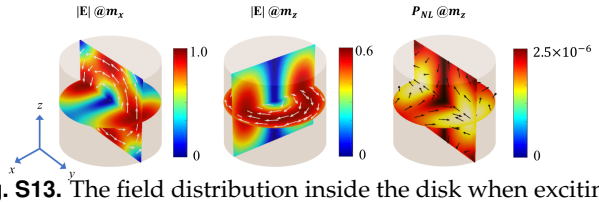

Fig. S13. The field distribution inside the disk when exciting (a) m_x and (b) m_z at the signal and idler wavelengths, respectively. (c) The generated nonlinear polarization distribution.

while the electric dipole modes belong to the F_2 representation. The basis functions of the F_2 representation, corresponding to the direct product $F_1 \otimes F_1$ are $p_x \propto m_y m_z$, $p_y \propto m_x m_z$, $p_z \propto m_x m_y$ [8] in full agreement with the numerical calculations in Fig. S12. The states shown in Fig. S12(a,b) have the corresponding Schmidt number of 2, indicating a very strong correlation between the modes. More detailed symmetry analysis of the SFG process in dielectric nanoparticles can be found in Ref. [9].

The fields inside the disk are illustrated in Fig. S13(a,b). As can be seen, m_x will generate E_y and E_z components and m_z will generate E_x and E_y components. The spatial distribution of the induced nonlinear polarization is shown in Fig. S13(c). Due to the strong overlap between the nonlinear polarization and the high-Q resonance at around 775 nm (as shown from the scattering efficiency in Fig. 1(c) of the main text), a further efficient SFG output will be achieved, associated with the excitation of this high-Q resonance at the SF wavelength, which is dominantly polarized along vertical direction (V-polarization) for signal/idler with m_x/m_z combination.

REFERENCES

1. A. N. Poddubny, I. V. Iorsh, and A. A. Sukhorukov, "Generation of photon-plasmon quantum states in nonlinear hyperbolic metamaterials," Phys. Rev. Lett. **117**, 123901–6 (2016).
2. F. Lenzini, A. N. Poddubny, J. Titchener, P. Fisher, A. Boes, S. Kasture, B. Haylock, M. Villa, A. Mitchell, A. S. Solntsev, A. A. Sukhorukov, and M. Lobino, "Direct characterization of a nonlinear photonic circuit's wave function with laser light," Light. Sci. Appl. **7**, 17143 (2018).
3. C. P. McPolin, G. Marino, A. V. Krasavin, V. Gili, L. Carletti, C. De Angelis, G. Leo, and A. V. Zayats, "Imaging electric and magnetic modes and their hybridization in single and dimer algaas nanoantennas," Adv. Opt. Mater. **6**, 1800664 (2018).
4. G. Marino, C. Gigli, D. Rocco, A. Lemaître, I. Favero, C. De Angelis, and G. Leo, "Zero-order second harmonic generation from algaas-on-insulator metasurfaces," ACS Photonics **6**, 1226–1231 (2019).
5. E. Bahar, U. Arieli, M. Mrejen, and H. Suchowski, "Coherent control of the non-instantaneous nonlinear power-law response in resonant nanostructures," arXiv **1909.06126** (2019).
6. P. G. Kwiat, K. Mattle, H. Weinfurter, A. Zeilinger, A. V. Sergienko, and Y. H. Shih, "New high-intensity source of polarization-entangled photon pairs," Phys. Rev. Lett. **75**, 4337–4341 (1995).
7. X. Guo, C. L. Zou, C. Schuck, H. Jung, R. S. Cheng, and H. X. Tang, "Parametric down-conversion photon-pair source on a nanophotonic chip," Light. Sci. Appl. **6**, e16249–8 (2017).
8. M. S. Dresselhaus, G. Dresselhaus, and A. Jorio, *Group Theory. Application to the Physics of Condensed Matter* (Springer, New York, 2008).
9. K. Frizyuk, D. Smirnova, I. Volkovskaya, A. Poddubny, and M. Petrov, "Second-harmonic generation in Mie-resonant dielectric nanoparticles made of noncentrosymmetric materials," Phys. Rev. B **99**, 075425 (2019).